



OPEN

Electronic and optical competence of TiO₂/BiVO₄ nanocomposites in the photocatalytic processes

K. T. Drisya^{1,2}, M. Solís-López¹, J. J. Ríos-Ramírez¹, J. C. Durán-Álvarez³, A. Rousseau², S. Velumani^{1,4}✉, R. Asomoza¹, A. Kassiba²✉, A. Jantrania⁵ & H. Castaneda⁴

Nanocomposites with different ratios of titanium dioxide and bismuth vanadate [TiO₂]/[BiVO₄] give rise to compatible electronic band structure alignment at their interfaces to ensure enhanced photoactivated charge transfer under visible light. The sol–gel method and suitable post-synthesis thermal treatments were used to synthesize different compositions with stabilized anatase phase of TiO₂ and monoclinic scheelite polymorph BiVO₄. Structural, electronic and optical characterizations were performed and the results were analysed as a function of the stoichiometry, in which both crystalline structures show a clear junction formation among their characteristic stacking planes. Photocatalytic and (photo) electrochemical responses of the nanocomposites were investigated and tested for the degradation of azo dyes (Acid Blue-113, AB-113) (~99%) under visible light radiation. The nanocomposite with a mass ratio of (1:10) shows the highest photocatalytic efficiency compared to the other compositions. HRTEM images showed marked regions in which both crystalline structures form a clear junction and their characteristic planes. However, the increase of BiVO₄ content in the network overcomes the photocatalytic activity due to the decrease in the reduction potential of the photo-generated electrons with high recombination rates.

Due to rapid increase in population and the world's rapid industrialization, natural water bodies are being heavily contaminated with industrial wastes^{1,2,3}. Pollutants present in the industrial effluents are classified as toxins, carcinogens, mutagens, teratogens, and endocrine-disrupting agents⁴. Particularly, the presence of dyes in industrial effluents leads to a decreased penetration of sunlight and a reduction of the photosynthetic activities in aquatic ecosystems, as well as an increase in the biochemical oxygen demand⁵. The dyes are specified as dispersive dyes (polyester, nylon and acetate)⁶, reactive dyes (*Safira dye*, *HEXL*)⁷, sulphur dyes, and vat dyes (viscous)⁸. The Azo dyes are colorants that fall under all of the above-mentioned categories. They contain one or more –N=N– groups in their chemical structure, which consists of highly substituted aromatic rings⁹. To ensure water purification, several known methods are well-established: desalination, distillation, filtration, flocculation, reverse osmosis, and sedimentation^{10,11}, etc. However, the chemical structure of azo dyes leads to recalcitrant characteristics, i.e., they degrade slowly under natural conditions, and they are also resistant to conventional wastewater treatment processes⁶. For this reason, Advanced Oxidation Processes (AOPs), have received a widespread attention in recent years, since they are a very convenient water treatment method that eliminates these types of contaminants^{5,7}. Among AOPs, photocatalysis is considered as a green alternative to attain an efficient purification of polluted water^{12,13}. Furthermore, the implementation of photoactive nanomaterials in water treatment show outstanding results, Their high specific surface area enhances both the anti-microbial activity and the electrochemical attributes, consolidating a solar assisted disinfection/decontamination process^{14–16} with an effective quality monitoring.

In this context, TiO₂ is known as the most efficient photocatalyst compared to other photoactive metal oxides. Also, it is widely used considering its low cost and stability¹⁷. However, its wide band gap allows solely

¹Department of Electrical Engineering (SEES), Centro de Investigación y de Estudios Avanzados del Instituto Politécnico Nacional (CINVESTAV-IPN), Av. Instituto Politécnico Nacional 2508, Col. San Pedro Zacatenco, Mexico CP 07360, Mexico. ²Institute of Molecule and Materials of Le Mans UMR-CNRS 6283, Le Mans University, 72085 Le Mans, France. ³Instituto de Ciencias Aplicadas y Tecnología, Universidad Nacional Autónoma de México, Circuito Exterior S/N, Ciudad Universitaria, P.O. Box 70-186, CP 04510 Coyoacán, Ciudad de Mexico, Mexico. ⁴Department of Materials Science and Engineering, Texas A&M University, College Station, TX 77843, USA. ⁵Department of Biological and Agricultural Engineering, Agrilife Extension, Texas A&M University, College Station, TX 77843, USA. ✉email: velu@cinvestav.mx; kassiba@univ-lemans.fr

UV radiation harvesting, which represents only about 5% of the solar spectrum¹⁸. Therefore, in order to maximize the benefits obtained from visible spectrum of sun light several strategies have been explored to suitably engineer the bandgap of TiO₂, exclusively devoted for water purification. In particular, a promising strategy is the realization of a heterogeneous photocatalyst by means of associating TiO₂ (TO) with other semiconductors, active in the visible-light, such as : BiVO₄, Fe₂O₃, GaP, or GaAs¹⁹.

Bismuth vanadate (BiVO₄), is a less expensive²⁰ photocatalytic material with a band gap of 2.4 eV, able to harvest visible light for photocatalysis^{10,19} as explored and reported in our former works on pure ball-milled and doped BiVO₄^{21–25}. Among the three polymorphs of BiVO₄, the monoclinic scheelite structure (m-BiVO₄) was synthesized by the sol–gel method and it was found to exhibit the highest photocatalytic activity under visible radiation²⁶. The synthesis methods and the annealing temperatures modulate the morphology, crystalline quality, grain size and photoactivity of BiVO₄ photocatalyst²⁷. However, even by using optimized synthesis and treatment conditions, pure BiVO₄ show a limited photocatalytic activity as for example the low degradation rate of dyes in water about 34%²⁸. Since TiO₂ is a very good adsorbent in the UV region with a compatible electronic band structure compared to that of the visible light active BiVO₄, the realization of heterostructure assemblies may induce synergetic effects for an efficient photocatalysis. The approach was experienced to form new nanocomposites by combining two different semiconductors with compatible band structures for efficient charge transfer at the interfaces^{29,30,31}. Yang et al. has identified the combination of different semiconductors to form junctions is a good strategy to have efficient charge transfer process and hence reduces the fast recombination rate in the structures and hence allows to have good efficiency^{32,33}.

In this work, BiVO₄/TiO₂ nanocomposites with different compositions were synthesized by modified one-step sol–gel method. The morphology, the crystal structure, the electronic and optical properties were exhaustively investigated and analysed as function of the synthesis and treatment conditions. Photocatalytic investigations were carried out on model solutions with azo dyes^{34–38} such as Acid Blue 113 and the efficiency of the dye's degradation is evaluated and discussed as function of the features of the nanocomposites. It has been observed that these novel BiVO₄/TiO₂ nanocomposites with good crystalline behaviour and visible light absorption are highly efficient in the photocatalytic degradation and has shown above 80 percentage of degradation within 20 min of visible irradiation with a composite dosage of 1 g/l. With an increased concentration of 5 g/l of the nanocomposite, it is observed a complete degradation of the organic azo dye Acid blue 113. This rapid activity without using any scavengers makes this composition attractive for water treatment. Also, electrochemical measurements were carried out for a consistent analysis of the electronic structure of the heterostructures for first time. Open circuit potential (OCP) measurements performed under visible light were analyzed to understand the charge transfer mechanism and the stability of the photo-generated charge carriers. The Transmission electron micrographs with the numerically simulated planes is in good agreement with the experimentally observed alignment corresponding to the formation of the heterojunction structures of the synthesized materials.

Experimental details

Chemicals. Bismuth nitrate penta-hydrate (Bi(NO₃)₃·5H₂O) ≥ 98.0%, ammonium metavanadate (NH₄VO₃) ≥ 99.0%, anatase titanium dioxide nano powder (TiO₂) < 25 nm, 99.7%, citric acid < 99.5%, HNO₃ (68%) ammonium hydroxide (NH₄OH) with a 28–30% NH₃ basis, and Acid blue 113 (50%) were purchased from Sigma-Aldrich Corporation and used as it is without further purification.

BiVO₄ preparation. BiVO₄ nanoparticles were prepared by the sol–gel method by using 0.01 mol Bi(NO₃)₃·5H₂O dissolved in 50 ml of HNO₃ (10%) and adding 0.02 mol of citric acid. The mixture was kept under stirring until a colourless solution was observed (solution A). In a different beaker, 0.01 mol of NH₄VO₃ was dissolved in 50 mL of deionized water and then heated at 80 °C with magnetic stirring until a clear lemon-yellow solution was obtained. Subsequently 0.02 mol of citric acid was added, until a brown solution was obtained (solution B). The solution A was then added dropwise to the solution B leading to a final mixture with an intense blue coloration. Followed by the pH adjustment with a NH₄OH solution, until the mixture reached a pH of 6.5. Then the mixture was kept under constant stirring at the same temperature until the gel formation, which was afterward dried at 100 °C overnight. The obtained powder was calcinated for 2 h at 500 °C and finally ground and kept in a desiccator prior to its characterization and use in photocatalytic tests.

Nanocomposite synthesis. Three BiVO₄/TiO₂ composites with different nominal molar ratios were selected from our previous experience and fixed to 1:1.0, 1:2.5 and 1:0.6. The different ratios were prepared by maintaining a constant concentration of bismuth vanadate in the precursor (section "BiVO₄ preparation") and changing the amount of the added titanium dioxide. The procedure for the synthesis of the nanocomposites was conducted according to the BiVO₄ synthesis protocol. Prior to the pH adjustment stage, the anatase mass corresponding to the ratio to be synthesized (1:1.0, 1:2.5 and 1:0.6) was incorporated (Fig. 1). Subsequently, the mixture was placed in an ultrasonic bath for 30 min to allow the components of the mixture to blend perfectly. Next, pH adjustment, drying, and calcination of the sample were performed as outlined in the previous section.

Characterization techniques. The structural characterizations of the synthesized samples were performed using X-ray powder diffractometer (Bruker-D2 Phaser) at 30kv with Cu Kα radiation (λ = 1.5418 Å). The diffraction patterns were recorded as a function of 2θ ranging from 10° to 80° with a step interval of 0.02°. Using the diffraction line width (FWHM) we can estimate the size (D) of crystalline domains through Scherrer's equation:

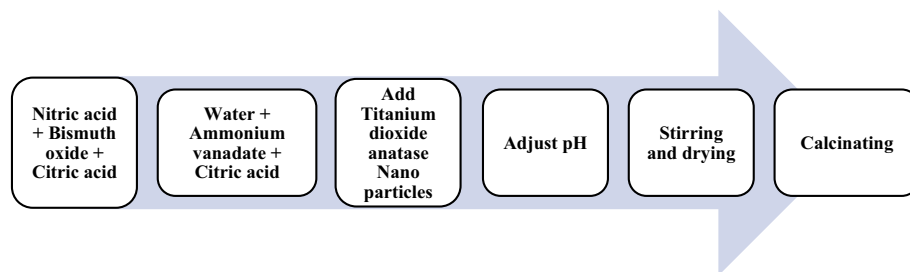


Figure 1. Method used to synthesize nanocomposites of $\text{BiVO}_4/\text{TiO}_2$.

$$D = K\lambda/\beta\cos(\theta) \quad (1)$$

where D is the crystallite size, K is the shape factor with a value close to unity, λ is the X-ray wavelength, $\text{Cu K}\alpha = 0.154 \text{ nm}$, β is the full width half maxima (FWHM) of peak at particular plane in radians and θ is the Bragg angle. Raman spectral studies were performed with an aim to characterize the vibrational properties of the composites. Raman spectra were recorded between 80 and 1000 cm^{-1} on a Horiba–Jobin–Yvon spectrometer (Lab RAM HR800), with an excitation radiation from He–Ne laser ($\lambda = 632.8 \text{ nm}$).

The morphological properties of the powders were investigated by means of Scanning Electron Microscopy (SEM). Powder samples were dispersed ultrasonically in methanol. A few drops of the dispersion were dried directly on carbon tape to carry out the SEM analysis (MIRA3 TESCAN; accelerating voltage 10 kV). The compositions were analysed using an Energy Dispersive X-ray Spectrometer (EDS) coupled with the SEM. Optical absorbance spectra of the samples were done with an UV–Vis spectrophotometer (Agilent Carry 5,000). The specific surface area was evaluated by the Brunauer–Emmett–Teller (BET) method on a Quantachrome Autosorb 1. Before nitrogen adsorption, the materials were dried and outgassed at room temperature for overnight. The morphological and grain analysis of the nanocomposites have been carried out using the JEOL JEM 2,100 h Transmission Electron Microscope (Jeol Ltd. Tokyo, Japan).

The obtained TEM images were mapped to extract the FFT pattern over all the grain area shown. For the TEM image that show a clear overlap in between two nanocomposites, the FFT pattern over all the image was extracted. The entire area was divided into regions, depending on the bright and dark channels that show the crystalline growth. Only when a certain region showed a single result of atomic plane spacing, in the calculated FFT, that area is assigned to the characteristic crystalline plane of either BiVO_4 or TiO_2 , depending on the plane distance value reported in their respective diffraction card. To correlate this result with a computational model two slabs were generated by means of the BIOVIA Materials Studio Package, with the crystalline structure defined by both lattice parameters and space groups from BiVO_4 and TiO_2 . The graphical resemblance along with the unitary slab thickness, extracted from the simulated crystal, cleavage parallel to the FFT calculated planes, shows that the mapped area belongs to a single crystalline phase.

Photoelectrochemical characterization. Thin films were deposited through a suspension of the material in Nafion-ethanol solution. An aliquot of each material was dispersed over 0.24 cm^2 ITO substrates, previously cleaned in acetone and water. All films were dried at room temperature for 24 h . Electrochemical determinations were performed in a conventional three-electrode cell. $\text{Ag}/\text{AgCl}/3 \text{ M KCl}$ electrode was used as the reference electrode [$\text{EAg}/\text{AgCl}/3 \text{ M KCl} = 0.210 \text{ V}/\text{SHE}$]. The counter electrode was a graphite rod (99.9995% pure, Alfa Aesar) and the prepared films on ITO substrates were used as a working electrode. NaClO_4 (0.05 M) solution was used as the supporting electrolyte. The illumination was performed using a Newport Q Housing (Model 60025) equipped with a visible light lamp. The semiconducting properties of the films were estimated from the Mott–Schottky plots. The space charge capacitance of the film was potentiodynamically measured in the dark ($v = 20 \text{ mV s}^{-1}$ at a frequency of 100 Hz). EIS measurements were performed at open circuit potential in the dark and under illumination in a frequency window between 100 kHz and 100 MHz with AC voltage of $\pm 10 \text{ mV}$ (peak to peak). For the (photo)electrochemical measurements an Autolab PGSTAT 302N potentiostat was used.

Photocatalytic tests. The photocatalytic activity of the pure TiO_2 , BiVO_4 and $\text{BiVO}_4/\text{TiO}_2$ nanocomposite was studied with the help of a full reflective solar simulator equipped with a 1.6 kW Xenon Arc Ozone free lamp (SCIENCETECH VHE-NL-200). In the first step, the sample with the highest photocatalytic activity was selected using Pyrex glass vessels that contained 100 ml of the AB113 solution with an initial concentration of 40 mg/l , along with the amount of the nanocomposite required to obtain a concentration of 1 g/l . Before irradiation, the sample was stirred in order to reach an adsorption–desorption equilibrium. Afterwards, the suspension was constantly stirred for two hours until the reaction lasted. About 3 ml aliquot of the dye solution was withdrawn after a specific time interval, then the samples were filtered and their absorbance was recorded at $\lambda_{\text{max}} = 568 \text{ nm}$ (AB113) using a UV–visible spectrophotometer (Jasco V-670). The initial pH of the dissolution was 6 and no adjustment was made to this parameter. Once the selection of the material with the highest photocatalytic activity was made, the effect of the initial dose of the photocatalyst ($1, 2, 3, 4$ and 5 g/l), and the initial

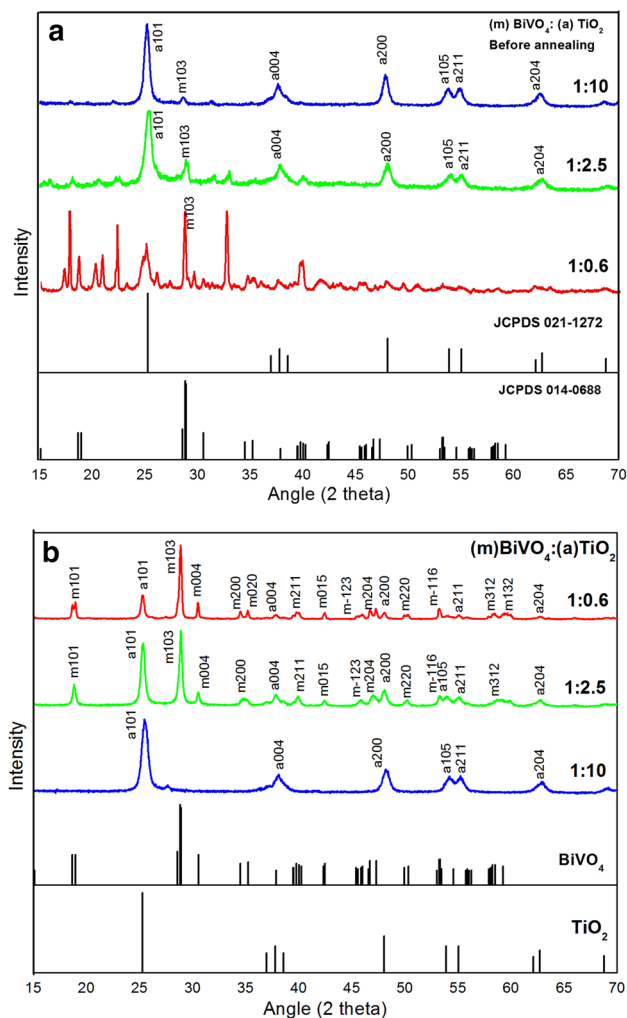


Figure 2. XRD patterns of the nanocomposites (a) before and (b) after calcination, compared with those of pure anatase TiO₂ (JCPDS 00-021-1272) and sol-gel synthesized m-BiVO₄ (JCPDS-00-075-1866). Prior to the calcination of the samples, the refinement of the patterns shows the formation of orthorhombic phase of BiVO₄.

concentration of the dye (20, 40 and 80 mg/l) in the removal process was studied. The percentage of removal was calculated by using the following equation:

$$\text{Dye removal(\%)} = 100[C_0 - C(t)]/C_0 \quad (2)$$

where C_0 and $C(t)$ represent respectively the initial dye concentration and that at time t of irradiation.

Results and discussion

Structural, surface morphological and optical characterizations. XRD patterns of the BiVO₄-TiO₂ nanocomposites before and after calcination are illustrated in Fig. 2. The refinement of XRD patterns shows that, before calcination of the samples, an orthorhombic phase of BiVO₄ was formed (Fig. 2a). The XRD patterns (Fig. 2b) are related to the nanocomposites after calcination, compared with those of pure anatase TiO₂ and sol-gel synthesized m-BiVO₄. The XRD results show that, after calcination of the samples, the orthorhombic phase of BiVO₄ was completely transformed into the monoclinic phase with reference to BiVO₄ (JCPDS00-075-1866) and TiO₂ (JCPDS 00-021-1272), results that match with those already reported¹¹. The diffraction peaks of nanocomposites (1:10, 1:2.5, and 1:0.6) indicate the reflections related to the anatase structure, with the planes (101), (004), (200), (211), and (204) corresponding to the 2θ values: 25.28, 37.80, 48.04, 55.06 and 62.68, respectively. Concerning m-BiVO₄, it is possible to identify the planes (101), (103), (015) and (220) of m-BiVO₄ (JCPDS-00-75-1866), corresponding to the 2θ values 18.67, 28.6, 42.49 and 50.33. The different diffraction lines exhibit a high intensity and a narrow line width, which are indicative of good crystalline features.

Before and after calcination, all the samples show the characteristic peaks of anatase TiO₂, which is an evidence for the stability of this structure within the samples. Prior to the calcination, the samples with the molar ratios of 1:2.5 and 1:10 show the peaks of anatase TiO₂ as well as those of an orthorhombic phase (PDF-01-075-1418). However, before the calcination, the 1:0.6 sample exhibits both an orthorhombic phase (PDF-01-086-0392)

Sample	2 theta	FWHM	Crystallite size (nm)	Dislocation density
0.2:0.8	25.522	0.752	10.83	8.53
0.5:0.5	25.332	0.491	16.56	3.64
0.8:0.2	25.305	0.280	29.06	1.18

Table 1. Calculated crystal properties of the nanocomposite after calcination.

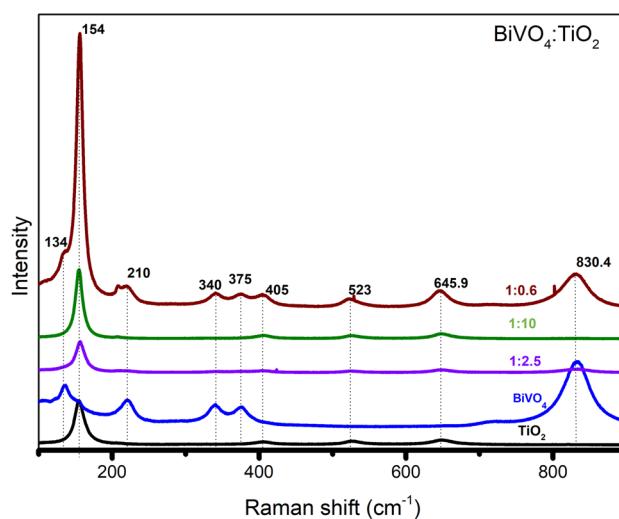


Figure 3. Raman spectra of TiO_2 , BiVO_4 and its various compositions.

and a bismuth vanadium oxide phase, confirming the fact that at lower temperatures there is formation of other phases beside the monoclinic one³⁹. Concerning the samples that were calcinated at 500 °C, pure monoclinic BiVO_4 was stabilized. It can be observed that, prior to the calcination, the 1:10 sample shows the very fine peaks that correspond to the orthorhombic phase of the BiVO_4 , whereas, after calcination, as shown in the Fig. 2b there is a dramatical decrease in the signal of m- BiVO_4 . This could be attributed to the difference that exists in the amount of TiO_2 present in the nanocomposite compared to that of BiVO_4 . Moreover, based on the STEM results obtained, TiO_2 particles tend to cover BiVO_4 particles, which produces an attenuation of the BiVO_4 signals present in the X-ray pattern.

Prior to the calcination process, the estimated crystallite size values establish no correlation with respect to the mass ratios of the samples (17.5, 22.08 and 21.06 nm for the 1:10, 1:2.5 and 1:0.6, respectively) this effect suggests that the nanoparticles with the orthorhombic BiVO_4 structure, were sintered and grown during the phase transition into a monoclinic form⁴⁰.

The crystallite size of the nanocomposites was calculated (Table 1) after calcination and it is observed that there seems to have a tendency of decrease in the crystallite size with the decreased stoichiometry of the BiVO_4 considering its higher atomic radius. And hence the dislocation density has increased which could lead to the increase in the number of crystallites per unit area in the material.

The Raman spectra of the nanocomposite samples with different $\text{BiVO}_4/\text{TiO}_2$ ratios are shown in Fig. 3. Among the Raman active modes, the peaks at 158 cm^{-1} and 523.3 cm^{-1} are assigned to the E_g (147 cm^{-1}) and A_{1g} (519 cm^{-1}) modes respectively, along with a 645.9 cm^{-1} (640 cm^{-1}) signal, all from TiO_2 anatase³⁸. On the other hand, the bands located at 346, 375, and 846 cm^{-1} closely match with the reference by Thalluri et al. for m- BiVO_4 (340, 375 and 830.4 cm^{-1})⁴² observed the shifts for the m- BiVO_4 at 340, 375 and 830.4 cm^{-1} ²¹.

The intensity of the Raman shifts at 210, 340, 375, 645.9, and 830.4 cm^{-1} increases with the content of BiVO_4 . From this set of signals, both 325 and 367 cm^{-1} correspond to the bending modes of the VO_4 groups, meanwhile, the peak at 830.4 cm^{-1} is attributed to the symmetric stretching of the V–O bond within BiVO_4 ^{21,25}. Finally, the Raman mode at 154.8 cm^{-1} has a remarkable inconsistency, for the 1:0.6 sample its small intensity can be attributed to a lower content of TiO_2 , whereas, a slightly intense signal from the 1:10 ratio is due to its high TiO_2 content. The Raman mode at 154.8 cm^{-1} which corresponds to the TiO_2 has an inconsistent change, for the 1:0.6 ratio, the smaller peak can be attributed to the lower content of TiO_2 and that of 1:10 is little more intense where there is a high TiO_2 content. However, in the case of 1:2.5, the Raman band shows a high intensity, that could be due to the less effect from the BiVO_4 .

Surface morphological analysis (Fig. 4) were carried out for $\text{BiVO}_4/\text{TiO}_2$ nanocomposites as function of the molar ratio for all samples before and after calcination which illustrates the crystal organization. Non calcinated samples possess agglomerations with barely recognizable boundaries among particles, an image that changes, with well-defined boundaries after the calcination process (Fig. 4), in agreement with a similar phenomenon observed for titanate nanotubes at $T > 400$ ⁴³, associated to the coalescence of the particles during the calcination

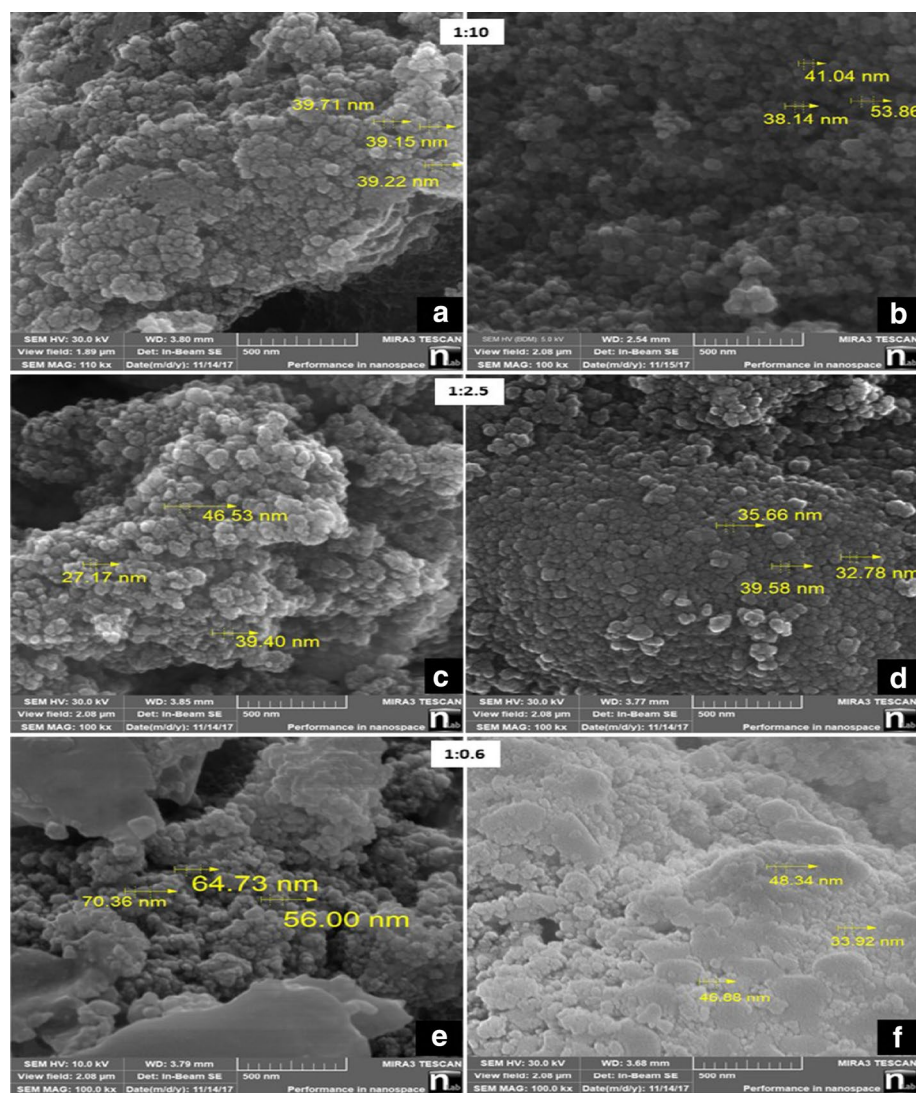


Figure 4. SEM images of the samples before and after calcination 1:10, 1:2.5 and 1:0.6 (a, c, e) before calcination (b, d, f) after calcination respectively.

process⁴¹. A similar morphology reported by Rahimi et al. for a $\text{BiVO}_4/\text{TiO}_2$ nanocomposite sample calcinated at 450°C ⁴⁵. The average particle size for the nanocomposite samples after calcination with ratios 1:10, 1:2.5, 1:0.6 were 44, 36 and 43 nm, respectively, and for the nanocomposite samples before calcination the obtained particle size was 39, 37 and 63 nm, respectively.

Figure 5 is the plot illustrating the calculated band gap of various nanocomposites and pure BiVO_4 and TiO_2 . The optical band gap values were calculated using the following equation¹⁸:

$$E_g = 1240/\lambda_g \quad (3)$$

The observed band gap value for m- BiVO_4 was 2.34 eV, and that of pure TiO_2 was 3.2 eV, in agreement with previous studies²⁴. The absorption range of the nanocomposites lies in between that the values of pure TiO_2 and that of m- BiVO_4 ⁴³. For all the nanocomposites with different ratios (1:10, 1:2.5, 1:0.6) we observed the shift in the band gap values for the nanocomposites⁴⁴. In the case of the nanocomposite with a high TiO_2 content, the band gap of the nanocomposite was close to the value of pure anatase, with a tendency of shifting towards the visible light range due to the presence of a higher fraction of BiVO_4 . As matter of fact, the band gap engineering of $\text{BiVO}_4/\text{TiO}_2$ shifts in the visible range as required for their efficient photocatalytic reactions. The observed band gaps for the synthesized ratios are summarized in Table 2. In the case of nanocomposites, each energy levels may have 'n' different energy levels, which is equal to the number of atoms interacting to each other. So in the case of nanocomposites, these bands may overlap and hence reduces the overall band gap^{47,48,49}.

The transmission electron micrographs of the nanocomposites are illustrated in Figs. 6 and 7. The morphology of the particles is similar to the spherical images obtained from scanning electron microscopy (Fig. 4). The

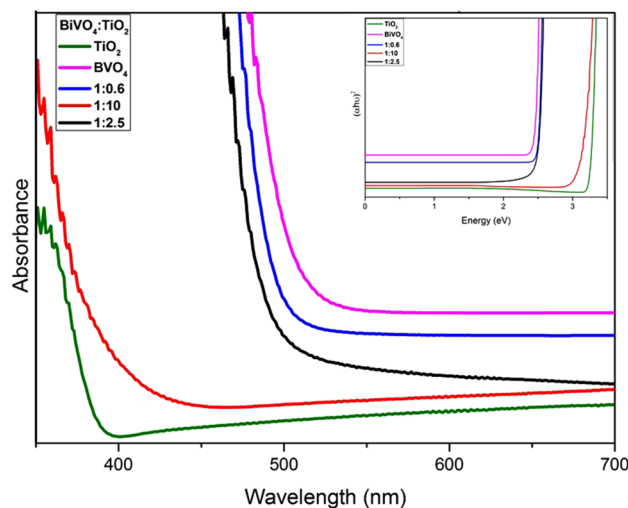


Figure 5. Comparison of the band gap energy of the synthesized nanocomposite samples with Anatase TiO_2 and synthesized monoclinic BiVO_4 nanoparticles with the Tauc plot in the inset.

Material	Bandgap (eV)
BiVO_4	2.34
TiO_2	3.20
1:10	2.96
1:2.5	2.43
1:0.6	2.42

Table 2. Calculated band gaps of BiVO_4 , TiO_2 and its various nanocomposites.

grains of composite material indicate the formation of heterojunctions associating with BiVO_4 and TiO_2 planes. All the reported micrographs show superimposed structures from BiVO_4 and TiO_2 compounds as clearly seen in EDS analysis performed on the different samples (Fig. 6B-e, C-c). In the dark and bright-field images, it is possible to see the different atomic mass contrasts (or Z contrast) involved in composites grains, even though in certain cases the contrast difference can result from the difference in the grain thickness. From Fig. 6A-a, the presence of the planes with different orientations can be seen. Figure 6A-b, the EDS analysis confirms the presence of all the elements in the composite. Figure 6A-c, FFT diffractions patterns, the planes (101), and (200) corresponding to the anatase phase of titanium dioxide and (002)³⁷ corresponding to the diffractions from the monoclinic bismuth vanadate system can be seen. Figure 6B-a shows a high-resolution image of sample 1:2.5 where the crystallographic planes are identified and are in agreement with the desired monoclinic and anatase phases (Fig. 6B-d). Figure 6B-d is the FFT for the sample 1:2.5 and there observed diffraction from the planes (103) that is from the monoclinic and the (101) corresponding to the anatase phase. Figure 6B-b, B-c are the bright and dark field micrographs where the atomic mass contrast is visible and Fig. 6B-e is the mapping analysis of the sample where the presence of each element is identified by the EDS (Fig. 6B-f). Figure 6C-a is the TEM micrograph of samples 1:0.6 and Fig. 6C-b is the EDS chemical analysis of the samples in which, presence of all Bi, Ti, O, and V elements can be identified. Figure 6C-d, C-e are the bright and dark field images with the Z contrast and corresponding chemical composition can be identified from the mapping analysis Fig. 6C-c, provides the evidence of the mixed composition from BiVO_4 and TiO_2 with a wide area of heterojunctions. This organization is expected to favor the photo-induced charge transfer process between the coexisting structures. All the planes observed in the FFT pattern of the TEM are in good agreement with peaks observed in the X-ray diffractogram (Fig. 2). Similarly, the diffraction images for the sample 1:0.6 (Fig. 6C-f), we observed significant diffractions from the monoclinic (103) and anatase (101). The plane (101) from the anatase corresponding to the angle 25.28° is observed in all the samples which are the significant planes. And the significant one for the monoclinic is the (103) at an angle of 28.6° and in the stoichiometry 1:10, the significant (103) plane is not visible in the diffraction image of the sample, and the same character is observed from the XRD of the sample; which attributes to the low composition of the Bismuth vanadate. The planes were identified using the standard JCPDS files used for the XRD analysis (BiVO_4 (monoclinic); JCPDS-00-075-1866 and TiO_2 (anatase); JCPDS-00-021-1272)¹¹. In all cases, the EDS and mapping (each element is identified inside the image) confirm the presence of both phases. And the synthesized materials have shown good crystallinity. The grain size from the TEM micrographs is found to be 94.82, 75, and 31.77 nms corresponding to the 1:0.6, 1:2.5, and 1:10 samples respectively. The observed large difference between the crystallite size obtained from the Scherrer calculations, which can be due to the

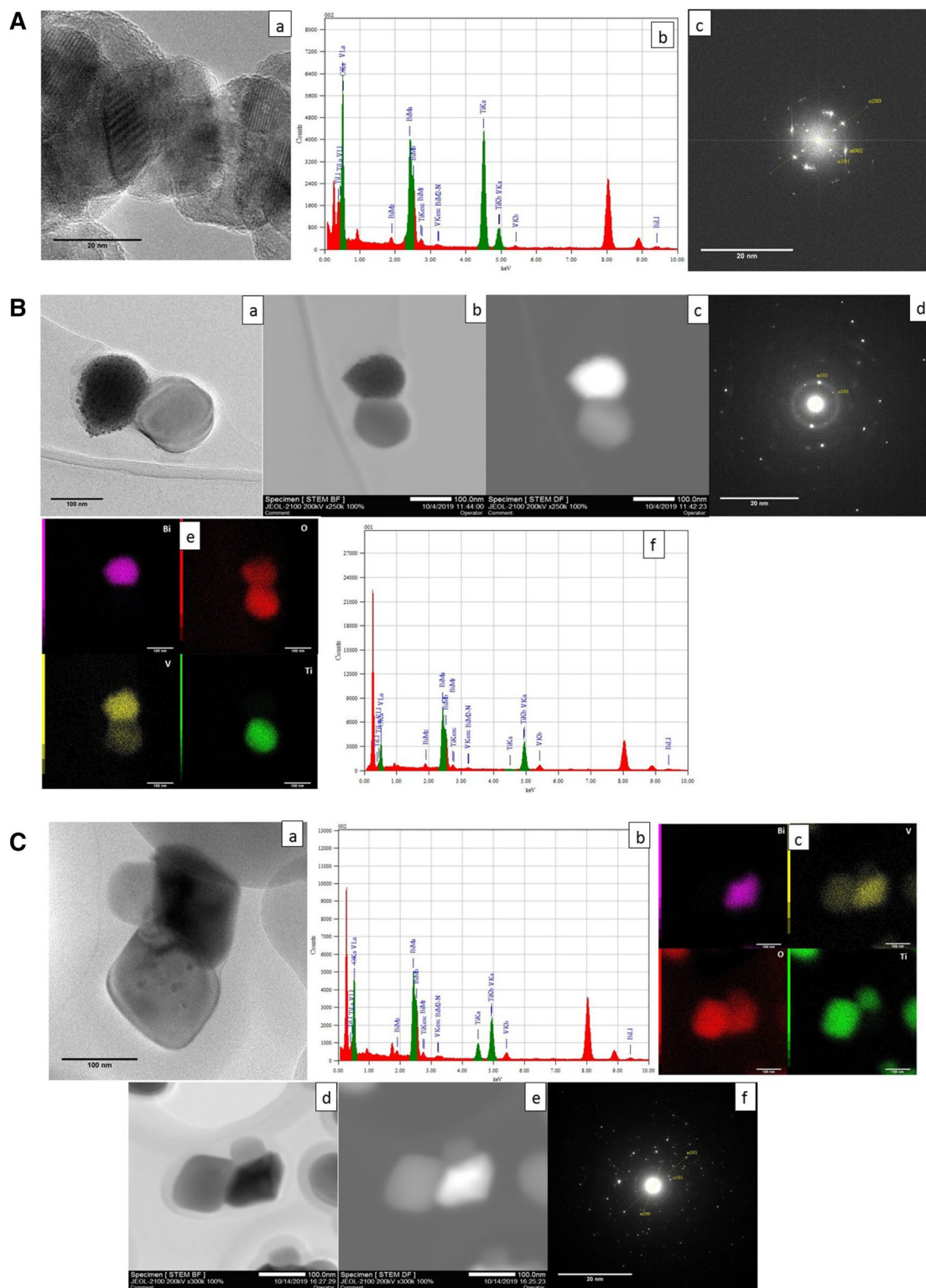


Figure 6. A Micrographs of the 1:10 nanocomposite (a) TEM micrograph (b) EDS chemical analysis (c) FFT diffraction pattern. B Micrographs of the 1:2.5 nanocomposite (a) TEM micrograph of isolated particles (b, c) bright and dark field analysis (d) FFT diffraction pattern (e) elemental mapping and (f) EDS analysis respectively. C Micrograph of the nanocomposite 1:0.6 (a) isolated particles (b) EDS analysis of the nanocomposite (c) elemental mapping of the nanocomposite, (d) bright-field image (e) dark-field image (f) FFT diffraction pattern.

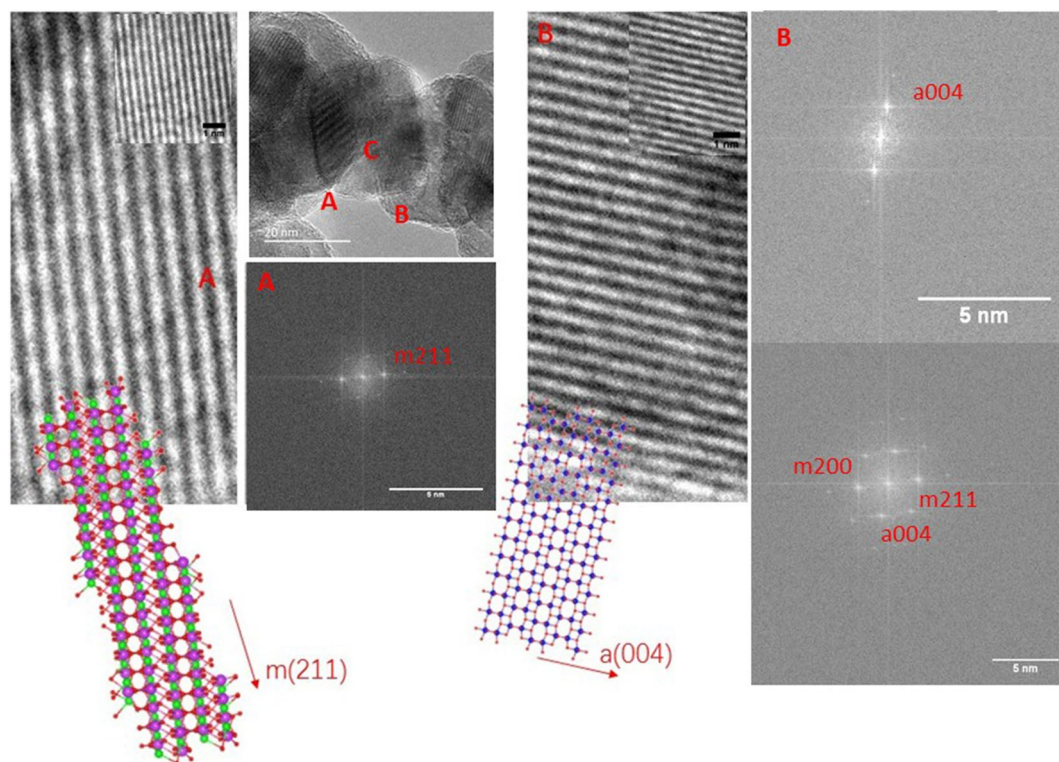


Figure 7. TEM micrograph, FFT planes and simulated crystalline models for the 1:10 composite. Regions (A), (B) and (C) corresponds to pure BiVO_4 , TiO_2 anatase and the junction of both crystalline phases, respectively.

formation of single large particles from a group of crystallites, and similar tendency can be seen from the large particles depicted by the SEM micrographs.

The clear distribution of the atomic planes, shown in the TEM image of the 1:10 composite, allows the mapping of the crystalline phases in each grain. In Fig. 7 there are three highlighted spatial regions with both pristine monoclinic BiVO_4 and anatase TiO_2 , in region A and B respectively. For the former case, the simulated FFT pattern shows a single plane spacing, associated to (221) of *m*- BiVO_4 equal to 2.26 Å, as reported for bismuth vanadate composites⁵⁰. Meanwhile, the associated (004) plane distance is found over the pristine TiO_2 , equal to 2.29 Å, as reported in anatase based nanocomposites⁵¹.

The simulated crystalline structures generated by the BIOVIA Materials Studio Package, show the monoclinic clinovisvanate (space group number 88; I2b) with a cleavage over the (211) plane, from the conventional unit cell containing four Bi, four V and eight O atoms. The stacking of the (211) planes grows along a perpendicular direction to the plane defined by the vectors $U [1 - 2 1]$ and $V [0 1 - 1]$, with a unitary thickness equal to 2.261 Å which is in excellent agreement with the graphically determined distance. On the other hand, the anatase phase of TiO_2 (space group number 141; I41amd) shows a stacking of (001) planes, parallel to the *c* lattice parameter of anatase, with an equivalent thickness equal to 2.372 Å, in agreement with the value determined by the FFT calculation. As a graphical aid both slab models are superimposed to their respective pristine regions of the TEM image. The slab model of the *m*(211) planes show empty channels surrounded by vanadium and bismuth atoms that match the brightest signals from region A, meanwhile, the lighter areas in the TEM image from region B could be assigned to the rings of Ti atoms along [100] and [010] directions. Such agreements support the association of the atomic plane distance to the crystalline phase at the pristine regions. However, in the portion indicated as C region the calculated plane distance in the FFT patterns evidence the junction formation since the characteristic planes from both crystalline phases appear together, as it was reported in bimetallic layered double hydroxides with MoS_2 in a stacking array⁵² as well as in core-shell nanoparticles composed by PdO/ZnO⁵³, where the presence of the interplane distances from the constituents in TEM images reveal the formation of effective coverages and an interface.

Photocatalytic activity measurements using AB113. The photocatalytic studies were conducted using the three ratios of the TiO_2 , BiVO_4 and $\text{BiVO}_4/\text{TiO}_2$ nanocomposites (1:10, 1:2.5 and 1:0.6). Initially, we kept the dye concentration at 40 mg/l and the nanocomposite concentration at 1 g/l with the pH fixed at 6 throughout the experiment. In these conditions, the 1:10 sample demonstrated the highest rate removal of AB113 (82%) after two hours of irradiation. The sol-gel synthesized BiVO_4 and the other molar ratios exhibited poor activity. Similar results were reported by Longo et al.⁵⁴, who synthesized the $\text{BiVO}_4/\text{TiO}_2$ nanocomposites using the hydrothermal method. They observed that the activity of the substance was directly proportional to the

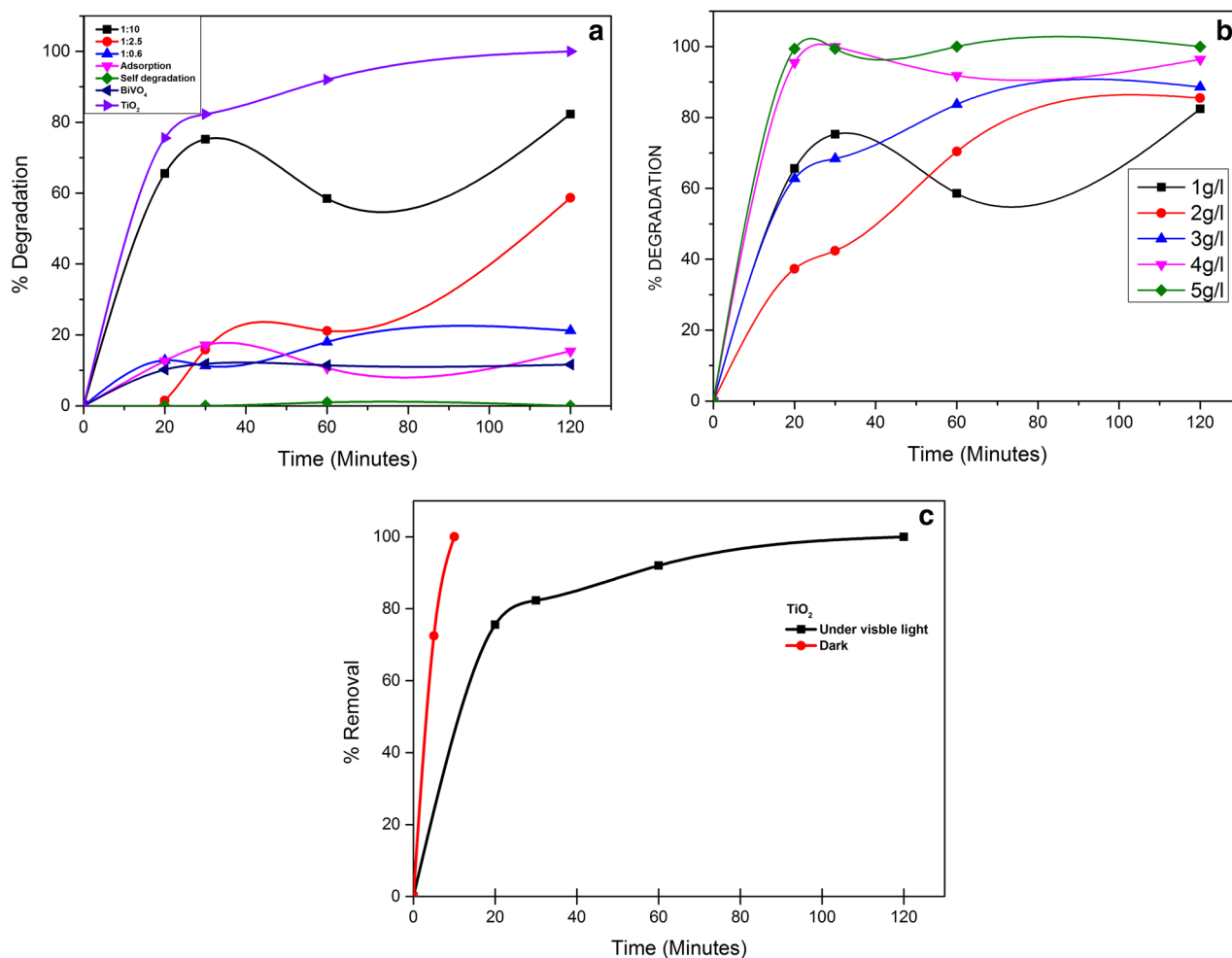


Figure 8. Photocatalytic degradation of AB113 (a) Adsorption and self-degradation plots along with the comparison of photocatalytic activity of TiO₂, BiVO₄ and the three nanocomposite ratios [AB113]₀ = 40 mg/l, [nanocomposite, TiO₂, BiVO₄] = 1 g/l pH₀ = 6. (b) [AB113]₀ = 40 mg/l, [nanocomposite] = 1–5 g/l pH₀ = 6 (c) Comparison of the activity of TiO₂ (Both adsorption and photocatalysis).

total amount of the used TiO₂. This behaviour was attributed to the low activity of BiVO₄ derived from its small specific surface area, 52, 56 and 44 m²/g for nanocomposites ratios 1:10, 1:2.5 and 1:0.6 respectively. This morphology influences the density of photogenerated charge carriers⁴⁶ due to the recombination process. The ratio 1:10 was selected to conduct the dye removal by photocatalytic reactions since this compound showed the best results with the lowest concentration of the nanocomposite material. According to Fig. 8a, as the concentration of the nanocomposite increases, the removal rate increases as well, so when a concentration of 40 mg/l is reached the concentration of AB113 is below the detection limit. The increase in the total amount of the catalyst increases the number of active sites on the nanocomposite surface which, in turn, increases the generation of 'OH radicals and hence the AB113 removal. This behavior was observed by other authors as well⁵.

The observed adsorption was of very less compared to the photocatalytic degradation and also there is no self degradation of the dye (Fig. 8a). Therefore, AB113 dyes removal can be attributed exclusively to the photocatalytic process using the nanocomposites compared to the performance of TiO₂ commercial samples in photocatalytic process. Comparing with the performance commercial samples of TiO₂ in photocatalytic process, the results show that there is a removal of 58.5 to a 76.4% which is attributed to the adsorption by the TiO₂ particles.

Concerning the effects of the initial concentration of AB113, the investigations show that, increasing the dye concentration from 20 to 40 mg/l lead to a higher percentage of dye removal. However, when the concentration was doubled (80 mg/l), we observed a decrease in the photocatalytic efficiency. The removal depends on both the dye concentration and the nanocomposite concentration. With a dye concentration of 40 mg/l, and a nanocomposite concentration of 5 g/l, we observed the maximum percentage of dye removal, 98.75%, after 10 min of visible light irradiation Fig. 8b. With a higher dye concentration, the active sites required for the 'OH production prove to be insufficient, i.e., it becomes necessary to increase the photocatalyst dose.

The reaction constant was determined from the corresponding kinetic plot from the reaction which follows pseudo-first order kinetics⁴¹.

Materials	E_{fb} vs (Ag/AgCl/3 M KCl) (V)
TiO ₂	- 0.95
1:10	- 1.01
1:2.5	- 0.84
1:0.6	- 0.33
BiVO ₄	- 0.69

Table 3. Flat band potential of synthesized materials.

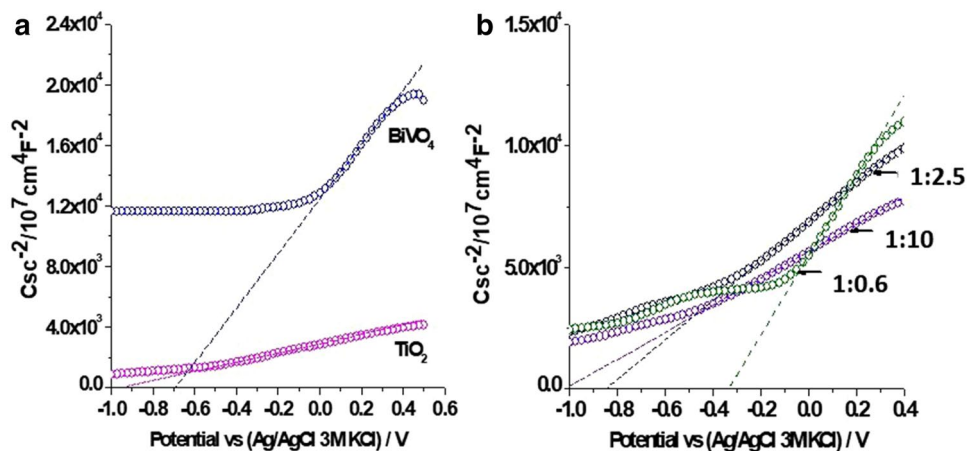


Figure 9. Mott-Schottky curves of (a) BiVO₄ and TiO₂ and (b) BiVO₄/TiO₂ nanocomposites (1:10, 1:2.5 and 1:0.6 molar ratio BiVO₄:TiO₂). The C_{sc} were obtained at 100 Hz in 0.05 M NaClO₄ aqueous solution.

$$\ln \frac{C}{C_0} = k_{obs} t$$

where C_0 and $C(t)$ are the initial and final concentrations of the AB113 dye molecules for a reaction time t . None of the sol-gel prepared nanocomposites surpasses the activity obtained with the TiO₂ under the used conditions. From the rate constants (k_{obs}), it can be inferred that the order for the photodegradation rate is: 1:100 > 1:2.5 ≈ 1:0.6. And the degradation observed by the TiO₂ is completely due to the adsorption process (Fig. 8c). The nanocomposite with a low relative amount of BiVO₄ appear as more interesting candidate to photocatalytic reactions under visible light, similar results were reported by Longo et al.⁵⁴. In order for BiVO₄ to act as a TiO₂ sensitizer, Longo et al. suggested that a good contact between both phases is necessary to ensure high interface area required for efficient charge transfer between both components.

The absorbance peak around 568 nm that represents the chromophore group present in the AB113 azo dye. Hence the quantification of the degradation percentage can be done by measuring this peak. It is reported that the hydroxyl ions are identified with good effect over the organic contaminants⁵⁵. Previous reports says that the discoloration is happening due to the formation of 1-naphthalenol and dibutyl phthalate as by products during the dye degradation. 1-naphthalenol is produced by the direct attack of the hydroxyl radicals on the azo group; whereas the dibutyl phthalate is formed by the effective attack of the hydroxyl radicals over the aromatic rings of the naphthalene. Both the aromatic by-products did not absorb along the visible spectrum and this can back the fact that the dye molecule has degraded and decolorized during the photocatalytic reaction⁵⁶.

Electrochemical properties of the material. The interaction between BiVO₄ and TiO₂ can change the properties of BiVO₄/TiO₂ nanocomposites and their charge transfer process. Thus, to obtain more detail about the interface of the materials, the electrochemical impedance spectroscopy is an excellent tool. The semiconducting properties of the films were based on electrochemical impedance spectroscopy and the flat band potential appearing as the x intercept of the linear portion of a Mott-Schottky curves (Table 3), the response of the materials correspond to n -type semiconductors (Fig. 9). The inter orbital overlap or the electronic connection between the two systems are defined and explained with the help of Mott-Schottky curves, The light irradiation can generate the electron hole pairs and depending on the density, a positive and negative charged region is created forming an interface which is supposed to be due to the Schottky effect⁵⁷. The Mott-Schottky curve is plotted (Fig. 9) with capacitance versus applied potential⁵⁸. Intercepts of these curves provide the flat band potential. And slope of the curves give the donor or acceptor intensity depending on the type of the semiconductor (p or n -type) since the slope will be positive for the n -type semiconductors and negative for the p -type semiconductors⁵⁷. Decrease in the slope indicates the increase in the donor density. Shift of the intercept towards

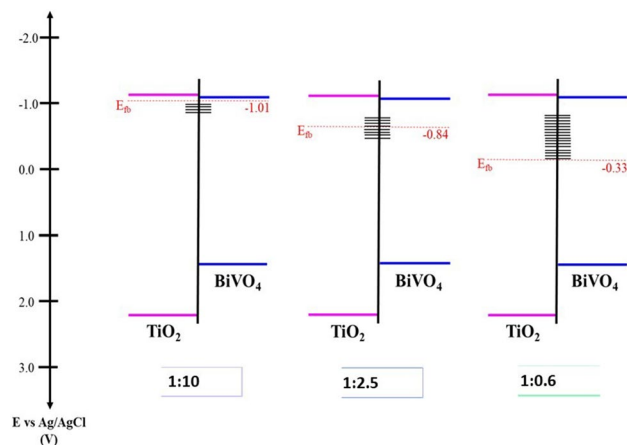


Figure 10. Energy diagram proposed for BiVO₄/TiO₂ nanocomposites (1:10, 1:2.5 and 1:0.6 molar ratio BiVO₄:TiO₂).

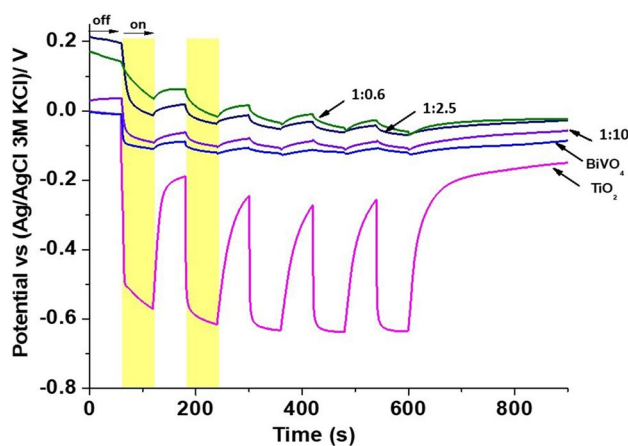


Figure 11. Time evolution of the open circuit potential (OCP) in the dark (off) and under UV illumination (on) for the synthesized nanocomposites.

the positive (Fig. 9) indicates an increase in the flatband potential⁴⁸. The flat band potential is known as the applied voltage when there is no band bending or depletion of the charge⁴⁹.

The value of E_{fb} for TiO₂ was -0.95 V, this value is more negative than the one reported in other work⁵⁹. However, it can be associated with the defects in the material influenced by the synthesis techniques. On the other hand, the E_{fb} for BiVO₄ was -0.69 V, this value is close to a previous report⁶⁰. For BiVO₄/TiO₂ nanocomposite, two different trends has been observed. First, in the nanocomposite with the lowest BiVO₄ content (1:10), E_{fb} was displaced toward more negative value compared with the pristine materials (-1.01 V). This behaviour is related to the formation of surface states at the interface of BiVO₄-TiO₂ heterojunction as it was also reported in other composite materials as ZrO₂/TiO₂, SnO₂/TiO₂ and WO₃/BiVO₄^{61,62,63}. It has been observed that there is an increase in the photocurrent, along with the increase in the applied potential, and Hong et al.⁵⁹ reported that this behaviour is unique for n-type semiconductors. Increase in the photocurrent increases the charge separation efficiency of the material⁶⁴. In BiVO₄/TiO₂ nanocomposites (1:2.5 and 1:0.6), a displacement of E_{fb} toward lowest negative values was associated with the high BiVO₄ content and the flat band alignment between BiVO₄ and TiO₂ (E_{fb} can provide information on the band positions of the semiconductor)⁶⁵. Based on the values of flat band potentials and optical band gap energies, Fig. 10 shows the energy diagram proposed by coupling the BiVO₄ and TiO₂.

Additionally, to evaluate the stability of the photo-generated carriers, open circuit potential (OCP) measurements under illumination of the synthesized materials were performed using visible light irradiation through 5 consecutive on-off cycles, previously bubbled with argon (Fig. 11). When the materials were irradiated, the OCP change toward more negative values confirms that the materials are n-type semiconductors which is supporting the observations from the Mott-Schottky plots; where observed an increased photocurrent with applied potential and also a further negative shift of the slopes. The results show that TiO₂ have the highest negative value of OCP. This is associated with a major potential to reduce the photo-generated electrons that favors the formation of the superoxide and hydroxyl radicals required for the oxidation process. On the other hand, BiVO₄ exhibits a lower

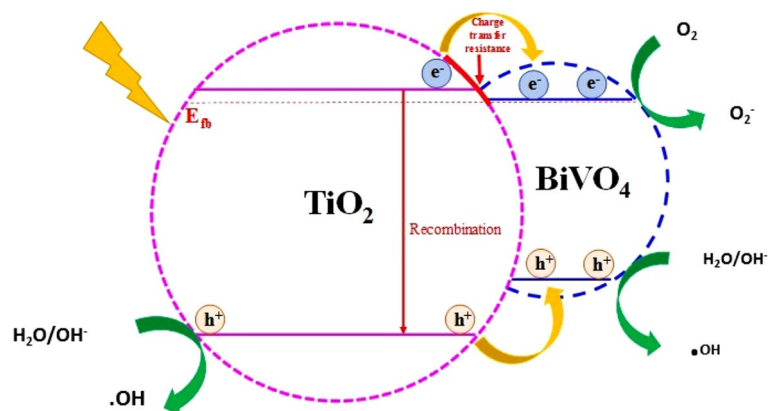


Figure 12. Scheme of $\text{BiVO}_4/\text{TiO}_2$ nanocomposite (1:10) and their interaction for spatial separation of photogenerated charge carriers.

negative value than TiO_2 indicating that the electrons are accumulated in lower energy levels, these results are in agreement with the Mott Schottky measurements. The results of $\text{BiVO}_4/\text{TiO}_2$ nanocomposites show that the electrons are localized in lower energy levels than in the case of the pristine materials. Such levels are associated with the formation of surface states at the interface of $\text{BiVO}_4/\text{TiO}_2$ with a high BiVO_4 content. In addition, when the illumination is interrupted, the OCP for BiVO_4 and $\text{BiVO}_4/\text{TiO}_2$ nanocomposites recovers more slowly than TiO_2 indicating that electrons are sluggishly transferred to species in the solution⁶⁶.

According to the above results, the photo-generated electrons are transferred from TiO_2 toward BiVO_4 and the reverse for the photo-generated holes⁶⁷. The photo-generated electrons in TiO_2 have a major potential of reduction that can reduce surface chemisorbed O_2 to yield strong oxidizing radicals (Fig. 12)⁶⁸. However, it is important to mention that the material with low BiVO_4 content exhibit the best behavior between the composites. This behavior is result of the flat band potential of the material and the potential reduction of its photogenerated electrons. Also, there observed an increase in the crystallite size of the nanocomposites with the increase in the concentration of the BiVO_4 due to its comparatively higher atomic radius. Hence the composite with low concentration of BiVO_4 (1:10) has shown a reduced crystallite size; resulted in more number of available crystallites per unit area and in addition to that, negative shift in the flat band potential which further provided more electrons for the reactions and improves the charge transfer properties of the material also contributed towards the good activity of the nanocomposites. The 1:10 ratio has shown a higher negative value for the flat band potential from other samples and also from the pristine materials this cause a significant difference in its photocatalytic efficiency. When the photons of sufficient energy incidents upon the catalyst surface, the electron hole pairs are created. Since the negative flatband potential provided a lower conduction band minima and hence the barrier is less for the charge separation and that favors more charge carriers over the surface of the material which will be available for the further redox reactions.

Conclusion

Visible light photoactive $\text{BiVO}_4/\text{TiO}_2$ nanocomposites were synthesized using a modified sol-gel methodology which is a low temperature process that ensured the homogeneity, purity and stoichiometry of the products. The synthesized particles exhibited a homogeneous morphology with small crystallites compared to the parent materials (BiVO_4 and TiO_2) and good visible light response with reduced band gap, made the composites to absorb the major region of the sunlight spectra. The TEM images show regions with preferential orientations from all the characteristic planes of the composite. Moreover, two associated slab models resemble the alternating bright and dark signal channels from the monocilic (211) and tetragonal (004) plane stacking, generated during the grain growth, and this overlapped planes from both BiVO_4 and TiO_2 supporting the junction formation since the bright channels overlap in the same area marked with both reflections and. The effect of the incorporation of BiVO_4 in the performance of the nanocomposite material under visible light was analyzed by synthesizing nanocomposites with the ratios $\text{BiVO}_4:\text{TiO}_2 = 1:0.6, 1:2.5, \text{ and } 1:10$ and, it is observed that an increase in the efficiency of the composite with decreasing BiVO_4 percentage. This behavior was associated to the low photocatalytic activity of BiVO_4 due to the fast recombination of the photogenerated electron-hole pairs. The electrochemical Mott-Schottky analysis confirmed the formation of n-type semiconductors. The 1:10 nanocomposite have exhibited a comparatively higher negative value for the flat band potential ($V_{fb} = -1.01$ eV) which further results from a lower conduction band minimum which reduced the barrier for the charge separation and hence the photocatalytic efficiency of the composite by improving the charge transfer process. The above effects contribute to the higher performance of the composite, 1:10 with a quasi-complete removal of dyes with a concentration of 5 g/l for 10 minutes of exposure under simulated visible light without the usage of any additional scavengers.

Received: 27 March 2020; Accepted: 24 June 2020

Published online: 11 August 2020

References

- UNICEF data: monitoring the situation of children and women (Updated on July 2017). <https://data.unicef.org/topic/water-and-sanitation/drinking-water/>.
- C&EN: cutting out the textile pollution (Issue Date: October 19, 2015). <https://cen.acs.org/articles/93/i41/Cutting-Textile-Pollution.html>.
- Mwinyihija, M. XVI, 140p (2010) Hard cover. <https://www.springer.com/978-1-4419-6265-2>.
- Fact sheet: oil refineries and toxic air pollution. https://earthjustice.org/sites/default/files/files/Refineries-Fact-Sheet_04-08.pdf
- Talebi, S., Chaibakhsh, N. & Shoeili, Z. M. Application of nanoscale ZnS/TiO₂ composite for optimized photocatalytic decolorization of a textile dye. *J. Appl. Res. Technol.* <https://doi.org/10.1016/j.jart.2017.03.007> (2017).
- Koh, J. In *Textile Dyeing* (ed. Hauser, P.) 195 (In Tech, Elbandy, 2011).
- Sauer, T., Cesconeto Neto, G., José, H. J. & Moreira, R. F. P. M. Kinetics of photocatalytic degradation of reactive dyes in a TiO₂ slurry reactor. *J. Photochem. Photobiol. A Chem.* **149**, 147–154 (2002).
- Kant, R. Textile dyeing industry an environmental hazard. *Asian Dye* **10**, 51–54 (2013).
- Josephine, G. A. S., Nisha, U. M., Meenakshi, G. & Sivasamy, A. Nanocrystalline semiconductor doped rare earth oxide for the photocatalytic degradation studies on Acid Blue 113: a di-azo compound under UV slurry photoreactor. *Ecotoxicol. Environ. Saf.* **121**, 67–72 (2015).
- Padmanabhan, P. V. A. *et al.* Nano-crystalline titanium dioxide formed by reactive plasma synthesis. *Vacuum* **80**, 11–12 (2006).
- Gaya, U. I. & Abdullah, A. H. Heterogeneous photocatalytic degradation of organic contaminants over titanium dioxide: a review of fundamentals, progress and problems. *J. Photochem. Photobiol. C Photochem. Rev.* **9**, 1–12 (2008).
- Zhu, X. *et al.* A shuriken-shaped m-BiVO₄/TiO₂ heterojunction: synthesis, structure and enhanced visible light photocatalytic activity. *Appl. Catal. A Gen.* **521**, 42–49 (2016).
- Lin, X. *et al.* Graphitic carbon nitride quantum dots loaded on leaf-like InVO₄/BiVO₄ nanoheterostructures with enhanced visible-light photocatalytic activity. *J. Alloys Compd.* **688**, 891–898 (2016).
- Qu, X., Brame, J., Li, Q. & Alvarez, P. J. J. Nanotechnology for a safe and sustainable water supply: enabling integrated water treatment and reuse. *Acc. Chem. Res.* **46**, 834–843 (2013).
- Bergmann, C. P., Machado, F. M. & Lima, E. C. *Carbon nanomaterials as adsorbents for environment and biological applications* (eds Bergmann, C. P. & Machado, F. M.) 1–10 (Springer, 2015).
- Iconaru, S. L. *et al.* Magnetite (Fe₃O₄) nanoparticles as adsorbents for As and Cu removal. *Appl. Clay Sci.* **134**, 128–135 (2016).
- Yang, R., Zhong, S., Zhang, L. & Liu, B. PW₁₂/CN@Bi₂WO₆ composite photocatalyst prepared based on organic–inorganic hybrid system for removing pollutants in water. *Sep. Purif. Technol.* **235** 116270. <https://doi.org/10.1016/j.seppur.2019.116270> (2020).
- Rehman, S., Ullah, R., Butt, A. M. & Gohar, N. D. Strategies of making TiO₂ and ZnO visible light active. *J. Hazard. Mater.* **170**, 560–569 (2009).
- Xi, G. & Ye, J. Synthesis of bismuth vanadate nanoplates with exposed 001 facets and enhanced visible-light photocatalytic properties. *J. Chem. Commun.* **46**, 1893–1895 (2010).
- Zhu, Z., Han, Q., Yu, D., Sun, J. & Liu, B. A novel p–n heterojunction of BiVO₄/TiO₂/GO composite for enhanced visible-light-driven photocatalytic activity. *Mater. Lett.* **209**(3), 379–383 (2017).
- Venkatesan, R., Velumani, S. & Kassiba, A. Mechanochemical synthesis of nanostructured BiVO₄ and investigations of related features. *Mater. Chem. Phys.* **135**(2–3), 842–848 (2012).
- Venkatesan, R., Velumani, S., Tabellout, M., Errien, N. & Kassiba, A. Dielectric behavior, conduction and EPR active centres in BiVO₄ nanoparticles. *J. Phys. Chem. Solids* **74**, 1695–1702 (2013).
- Merupo, V., Velumani, S., Oza, G., Makowska-Janusik, M. & Kassiba, A. Structural, electronic and optical features of molybdenum-doped bismuth vanadium oxide. *Mater. Sci. Semicond. Process.* **31**, 618–623 (2015).
- Merupo, V. *et al.* Structural and optical characterization of ball-milled copper-doped bismuth vanadium oxide (BiVO₄). *Cryst. Eng. Commun.* **17**, 3366–3375 (2015).
- Venkatesan, R. *et al.* Nanostructured bismuth vanadate (BiVO₄) thin films for efficient visible light photocatalysis. *Mater. Chem. Phys.* **205**, 325–333 (2018).
- Han, M. *et al.* BiVO₄ at γ-Bi₂O₃ core–shell p–n heterogeneous nanostructure for enhanced visible-light photocatalytic performance. *RSC Adv.* **3**, 24964 (2013).
- Meng, X. & Zhang, Z. *J. Mol. Catal. A Chem.* **423**, 533–549 (2016).
- Abdullah, A. H., Ali, N. M. & Tahir, M. I. M. *Malays. J. Anal. Sci.* **13**, 151–157 (2009).
- Xie, M., Feng, Y., Fu, X., Luan, P. & Jing, L. Phosphate-bridged TiO₂–BiVO₄ nanocomposites with exceptional visible activities for photocatalytic water splitting. *J. Alloys Compd.* **631**, 120–124 (2015).
- Zhu, Y., Shah, M. W. & Wang, C. Insight into the role of Ti³⁺ in photocatalytic performance of shuriken-shaped BiVO₄/TiO_{2-x} heterojunction. *Appl. Catal. B Environ.* **203**, 526–532 (2017).
- Wetchakun, N., Chainet, S., Phanichphant, S. & Wetchakun, K. Efficient photocatalytic degradation of methylene blue over BiVO₄/TiO₂ nanocomposites. *Ceram. Int.* **41**, 5999–6004 (2015).
- Yang, R. *et al.* One-step preparation (3D/2D/2D) BiVO₄/FeVO₄@rGO heterojunction composite photocatalyst for the removal of tetracycline and hexavalent chromium ions in water. *Chem. Eng. J.* **390**, 124522 (2020).
- Yang, R. *et al.* Facile synthesis and characterization of interface charge transfer heterojunction of Bi₂MoO₆ modified by Ag/AgCl photosensitive material with enhanced photocatalytic activity. *Mater. Lett.* **252**, 272–276 (2019).
- Srivastava, P., Goyal, S. & Patnala, P. K. Degradation of reactive, acid and basic textile dyes in the presence of ultrasound and rare earths [Lanthanum and Praseodymium]. *Ultrason. Sonochem.* **21**, 1994–2009 (2014).
- Sathishkumar, P. *et al.* Low frequency ultrasound (42 kHz) assisted degradation of Acid Blue 113 in the presence of visible light driven rare earth nanoclusters loaded TiO₂ nanophotocatalysts. *Ultrason. Sonochem.* **21**, 1675–1681 (2014).
- Shu, H. Y., Huang, S. W. & Tsai, M. K. Comparative study of acid blue 113 wastewater degradation and mineralization by UV/persulfate and UV/Oxone processes. *Desalin. Water Treat.* **57**, 1–14 (2016).
- Moura, D. C., Quiroz, M. A., Silvae, D. R., Salazar, R. & Huitlea, C. A. M. Electrochemical degradation of Acid Blue 113 dye using TiO₂-nanotubes decorated with PbO₂ as anode. *Environ. Nanotechnol. Monit. Manag.* **5**, 13–20 (2016).
- Jain, S. N. & Gogate, P. R. Acid Blue 113 removal from aqueous solution using novel biosorbent based on NaOH treated and surfactant modified fallen leaves of *Prunus dulcis*. *J. Environ. Chem. Eng.* **5**, 3384–3394 (2017).
- Zhang, W. F., He, Y. L., Zhang, M. S., Yin, Z. & Chen, Q. Raman scattering study on anatase TiO₂ nanocrystals. *J. Phys. D. Appl. Phys.* **33**, 912–916 (2000).
- Kudo, A., Omori, K. & Kato, H. J. A novel aqueous process for preparation of crystal form-controlled and highly crystalline BiVO₄ powder from layered vanadates at room temperature and its photocatalytic and photophysical properties. *Am. Chem. Soc.* **121**, 11459–11467 (1999).
- Frank, O. *et al.* Raman spectra of titanium dioxide (anatase, rutile) with identified oxygen isotopes (16, 17, 18). *Phys. Chem. Chem. Phys.* **14**, 14567–14572 (2012).
- Thalluri, S. R. M., Suarez, C. M., Virga, A., Russo, N. & Saracco, G. Insights from crystal size and band gap on the catalytic activity of monoclinic BiVO₄. *Int. J. Chem. Eng. Appl.* **4**, 305–309 (2013).

43. Yu, J., Su, Y. & Cheng, B. Template-free fabrication and enhanced photocatalytic activity of hierarchical macro-/mesoporous titania. *Adv. Funct. Mater.* **12**, 1984–1990 (2007).
44. Wang, W. *et al.* Enhanced photocatalytic degradation performance of organic contaminants by heterojunction photocatalyst BiVO₄/TiO₂/RGO and its compatibility on four different tetracycline antibiotics. *Adv. Powder Technol.* **30**(9), 1882–1896 (2019).
45. Li, N. *et al.* Inorganic chemistry frontiers high quality sulfur-doped titanium dioxide nanocatalysts with visible light photocatalytic activity from non-hydrolytic thermolysis. *Inorg. Chem. Front.* **7**, 521 (2014).
46. Rahimi, R., Zargari, S., Moghaddas, M. & Mahjoub, M. BiVO₄-TiO₂ nanocomposite: synthesis and photocatalytic investigation. *Adv. Mater. Res.* **702**, 172–175 (2013).
47. Lasia, A. Electrochemical impedance spectroscopy and its applications. *Electrochemical Impedance Spectroscopy and its Applications*. <https://doi.org/10.1007/978-1-4614-8933-7> (2014).
48. Bondarenko, G. A. & Ragoisha, A. S. Variable Mott–Schottky plots acquisition by potentiodynamic electrochemical impedance spectroscopy. *J. Solid State Electrochem.* **9**, 845–849 (2005).
49. Gelderman, K., Lee, L. & Donne, S. W. Flat-band potential of a semiconductor: using the Mott–Schottky equation. *J. Chem. Educ.* **84**, 685–688 (2007).
50. Selvarajan, S., Suganthi, A., Rajarajan, M. & Arunprasath, K. Highly efficient BiVO₄/WO₃ nanocomposite towards superior photocatalytic performance. *Powder Technol.* **307**, 203–212 (2017).
51. Surikanti, G. R., Bandarapu, A. K. & Sunkara, M. V. Facile one pot synthesis of Cu₂O@TiO₂: a nanocomposite catalyst for enhanced visible light driven photocatalysis. *ChemistrySelect* **4**, 2249–2257 (2019).
52. Nayak, S., Swain, G. & Parida, K. Enhanced photocatalytic activities of RhB degradation and H₂ evolution from in situ formation of the electrostatic heterostructure MoS₂/NiFe LDH nanocomposite through the Z-scheme mechanism via p–n heterojunctions. *ACS Appl. Mater. Interfaces* **11**, 20923–20942 (2019).
53. Majhi, S. M. *et al.* Construction of novel hybrid PdO–ZnO p–n heterojunction nanostructures as a high-response sensor for acetaldehyde gas. *CrystEngComm* **21**, 5084–5094 (2019).
54. Longo, G., Fresno, F., Gross, S. & Štancar, U. L. Synthesis of BiVO₄/TiO₂ composites and evaluation of their photocatalytic activity under indoor illumination. *Environ. Sci. Pollut. Res.* **21**, 11189–11197 (2014).
55. Wang, Y., Yu, D., Wang, W., Gao, P., Zhong, S., Zhang, L., Zhao, Q. & Liu, B. Synthesizing CO₃O₄-BiVO₄/g-C₃N₄ heterojunction composites for superior photocatalytic redox activity. *Sep. Purif. Technol.* **239** (2020).
56. De Moura, D. C., Quiroz, M. A., Da Silva, D. R., Salazar, R. & Martínez-Huitle, C. A. Electrochemical degradation of Acid Blue 113 dye using TiO₂-nanotubes decorated with PbO₂ as anode. *Environ. Nanotechnol. Monit. Manag.* **5**, 13–20 (2016).
57. Li, X. H. & Antonietti, M. Metal nanoparticles at mesoporous N-doped carbons and carbon nitrides: functional Mott–Schottky heterojunctions for catalysis. *Chem. Soc. Rev.* **42**, 6593–6604 (2013).
58. Zhang, W., Chen, Z. & Li, S. Dye-sensitized solar cells based on Bi₄Ti₃O₁₂. *Int. J. Photoenergy* **2011**, 3–8 (2011).
59. Hong, S. J., Lee, S., Jang, J. S. & Lee, J. S. Heterojunction BiVO₄/WO₃ electrodes for enhanced photoactivity of water oxidation. *Energy Environ. Sci.* **4**, 1781–1787 (2011).
60. Wang, H. *et al.* Electrochemical investigation of traps in a nanostructured TiO₂ film. *J. Phys. Chem. B* **105**, 2529–2533 (2001).
61. Ramirez-Ortega, D. *et al.* Energetic states in SnO–TiO structures and their impact on interfacial charge transfer process. *J. Mater. Sci.* **52**, 260–275 (2017).
62. Guerrero-Araque, D. *et al.* interaction between methanol and sulfite ions. *J. Photochem. Photobiol. A* **335**, 276–286 (2017).
63. Liu, C., Su, J. & Guo, L. Comparison of sandwich and fingers-crossing type WO₃/BiVO₄ multilayer heterojunctions for photoelectrochemical water oxidation. *RSC Adv.* **6**, 2755–27565 (2016).
64. Wang, Y. *et al.* Fabrication of BiVO₄/BiPO₄/GO composite photocatalytic material for the visible light-driven degradation. *J. Clean Prod.* **247**, 119108 (2020).
65. Resasco, J. *et al.* TiO₂/BiVO₄ nanowire heterostructure photoanodes based on type II band alignment. *ACS Cent. Sci.* **2**, 80–88 (2016).
66. Li, H. *et al.* Enhanced photocathodic protection performance of Ag/Graphene/TiO₂ composite for 304SS under visible light. *Nanotechnology* **28**, 22 (2017).
67. Obregon, S. & Colón, G. A ternary Er³⁺-BiVO₄/TiO₂ complex heterostructure with excellent photocatalytic performance. *RSC Adv.* **4**, 6920–6926 (2014).
68. Su, W. *et al.* Visible light photocatalysis on praseodymium(III)-nitratemodified TiO₂ prepared by an ultrasound method. *Appl. Catal. B* **77**, 264–271 (2008).

Acknowledgements

The authors wish to gratefully acknowledge the financial support provided by the CONACYT-SENER Project No. 263043 and SEP-CINVESTAV (Pro No. 200). One of the authors, KT. Drisya and M. Solís-López wish to thank CONACYT for the doctoral scholarship and postdoctoral grants resc. Also K.T. Drisya acknowledge the financial support from ED-3M doctoral school of Le Mans University. We would also like to express our gratitude to F. Alvarado-Cesar for the XRD and SEM characterization, and to Miguel Galvan Arellano for helping with the Raman analysis.

Author contributions

K.T.D., along with M.S.L. has been carrying out the experimental part including the synthesis of the nanocomposites and their application in the photocatalytic experiments and also did the analysis of the characterization results. J.J.R.-R. has contributed in the theoretical calculations using the Density Functional Theory. J.C.D.A. has done the photoelectrochemical characterizations and a part of its analysis. A.R. has contributed for the capturing of the TEM micrographs and helped in the interpretation and. S.V. who is the back bone of this research who made the availability of the resources for conducting this research and him along with R.A. have did a major contribution for the X-ray diffraction, UV-DRS and Scanning electron microscopy characterizations. A.K. has done the UV-Diffuse reflectance spectroscopic measurements and also made important theoretical contributions. A.J. along with H.C. have contributed towards the electrochemical analysis and calculations in the experimental part during the series of photocatalytic experiments and also all the authors have equally contributed towards the revision of the final version of the manuscript.

Competing interests

The authors declare no competing interests.

Additional information

Correspondence and requests for materials should be addressed to S.V. or A.K.

Reprints and permissions information is available at www.nature.com/reprints.

Publisher's note Springer Nature remains neutral with regard to jurisdictional claims in published maps and institutional affiliations.



Open Access This article is licensed under a Creative Commons Attribution 4.0 International License, which permits use, sharing, adaptation, distribution and reproduction in any medium or format, as long as you give appropriate credit to the original author(s) and the source, provide a link to the Creative Commons license, and indicate if changes were made. The images or other third party material in this article are included in the article's Creative Commons license, unless indicated otherwise in a credit line to the material. If material is not included in the article's Creative Commons license and your intended use is not permitted by statutory regulation or exceeds the permitted use, you will need to obtain permission directly from the copyright holder. To view a copy of this license, visit <http://creativecommons.org/licenses/by/4.0/>.

© The Author(s) 2020